International Journal of Mechanical Sciences 140 (2018) 211–227

Contents lists available at ScienceDirect

International Journal of Mechanical Sciences

journal homepage: www.elsevier.com/locate/ijmecsci

Characterization and computational modeling of electrical wires and wire bundles subject to bending loads

Ehsan Taghipour[a], Sai Siddhartha Vemula[a], Zhengdi Wang[a], Yitong Zhou[a], Hossein Qarib[b], Kushal Gargesh[c], Leon M. Headings[a], Marcelo J. Dapino[a], Soheil Soghrati[a,d,*]

[a] Department of Mechanical and Aerospace Engineering, The Ohio State University, USA
[b] Department of Civil Engineering, The Ohio State University, USA
[c] Honda R&D Americas, Raymond, Ohio, USA
[d] Department of Materials Science and Engineering, The Ohio State University, USA

ARTICLE INFO

Keywords:
Reduced-order model
Finite element method
Electrical wire
Optimization
Plasticity
Homogenization

ABSTRACT

A reduced-order finite element (FE) model is introduced for modeling the mechanical behavior of taped electrical wire bundles subject to bending loads, which can be used for digital manufacturing applications. We show that incorporating the plastic behavior of wires in this model is crucial to the accurate prediction of the deformed shape. A customized cantilever bending test is presented to quantify the force-deflection response of single wires and taped wire bundles and evaluate their homogenized elastoplastic properties using an optimization-based algorithm. A high-fidelity 3D FE model is also introduced, which can be used as a substitute for experimental testing. It is shown that after proper characterization of effective material properties, a 1D FE model can accurately predict the deformation response of a taped wire bundle subject to bending loads. Both 1D and 3D FE simulations presented in this work are validated with experimental data.

1. Introduction

Wire harnesses provide the required power and signals in electronic systems of automobiles, including electric (hybrid) engines, entertainment systems, audio units, switches, and lights. As shown in Fig. 1, a typical wire harness consists of electrical wires (often with stranded copper cores), tape, mounting clips, electrical connectors, and in some cases protective materials such as fabric tubes. The increasing demand for in-car electronics has led to a significant increase in the size and complexity of wire harnesses, which in turn increases the complexity of the design process. One of the main challenges toward the reliable design of these flexible structures is to ensure that no excessive force is applied to wires during the assembly process. Further, harness branches must have proper lengths and shapes after being mounted on the vehicle to avoid rattling and damage during their service life.

There is a high demand for a reliable software package to virtually model and design the assembly of wire harnesses in the automotive industry to reduce the number of prototypes and the associated cost. While there has been significant improvement in computer-aided design (CAD) tools and Virtual Reality (VR) environments, simulating the mechanical behavior of flexible harnesses is still challenging and outcomes may be far from the reality. Note that because electrical wires are often not considered as structural components, their mechanical behaviors are largely unexplored. This lack of knowledge on the material properties is one of the main challenges in the accurate simulation of wire harnesses. Further, the requirement to perform such simulations in real-time during the digital manufacturing process prohibits the application of high-fidelity 3D computational models. For example, creating a 3D finite element (FE) model of a full wire harness to simulate its mechanical behavior would result in a large-scale nonlinear model with thousands or millions of degrees of freedom. Thus, it is essential to implement a geometrically reduced-order model that can efficiently and accurately simulate wire harnesses during the installation process.

There are several models available to predict the mechanical behavior of slender and flexible objects such as structural cables and wire harnesses. The Cosserat theory of elasticity for rods [1] has been used to predict the mechanical behavior of rods and cables. Gregoire and Schomer [2] presented a model for simulating the bending and torsional response of 1D flexible structures by combining the Cosserat theory with a generalized mass-spring system. A constrained theory of a Cosserat point was developed for the numerical simulation of nonlinear elastic rods by Brand and Rubin [3]. A mass-spring system using oriented particles and generalized spring models was proposed by Jeong and Lee [4]. This

* Corresponding author.
E-mail address: soghrati.1@osu.edu (S. Soghrati).

https://doi.org/10.1016/j.ijmecsci.2018.03.009
Received 24 December 2017; Received in revised form 16 February 2018; Accepted 9 March 2018
Available online 10 March 2018
0020-7403/

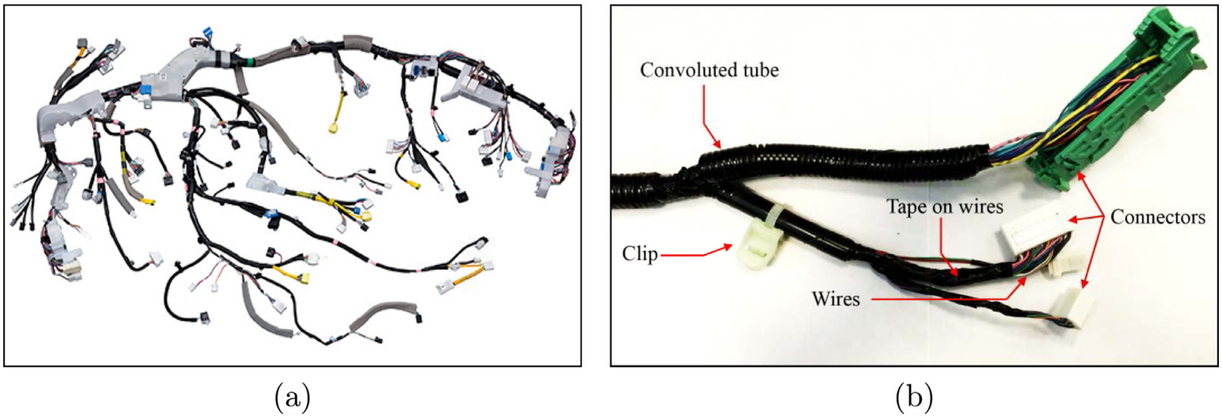

Fig. 1. (a) A typical automobile wire harness; (b) components of the harness.

model was used for fast prototyping and animating deformable objects subject to bending, twisting, and stretching.

Elastic continuum theory and FEM have been employed in several research efforts to study the tensile and bending behaviors of elastic wire ropes and cables [5–8]. Argatof [9] simulated the mechanical behavior of helical wire ropes subject to axial and torsional loads using an asymptotic approach relying on a 2D frictionless plain strain model for evaluating the effect of interwire contacts. Spak et al. [10] predicted the natural frequencies of electrical cables using beam models with homogeneous isotropic material properties. Pseudo-Rigid Body Model (PRBM) [11] is another analytical technique that has been used successfully for the reduced-order modeling of beam-like structures. A particle-based approach relying on the differential geometry, together with the Cosserat theory and the Finite Element Method (FEM), was implemented by Wakamatsu and Hirai [12] to simulate the linear elastic response of flexible objects. Theetten et al. [13] used geometrically exact energies with dynamic splines to develop a deformable model of 1D parts using an elastoplastic model.

A combined analytical-computational approach was adopted by Gautem et al. [14] to predict the torsional and flexural behaviors of hybrid composite armor wires with homogenized properties of over-braid sleeves and composite rods. The authors also investigated the effects of over-braid structural parameters, pretension, and internal friction between components on the mechanical response. Nemov et al. [15] compared the performance of analytical results and FE simulations versus experimental results for predicting the stretching and twisting responses of electrical conductors. Nikitin et al. [16] used FEM, together with pre-computed Green's functions, for the real-time simulation of the deformation of 3D elastic objects for interactive Virtual Environment (VE) applications. Stanova et al. [17] simulated the elastic behavior of multi-layered strands subject to tensile loads using FEM and validated the results with experimental data and analytical results.

A number of experimental studies were conducted to characterize the mechanical behavior of multi-stranded wire ropes [18,19] and transmission line electrical cables [20,21], which have a similar structure to electrical wires but do not include electrical insulation. Van der Heijden et al. [22,23] performed large deflection experiments on clamped metallic rods subject to torsion, tension, and bending. Dorlich et al. [24] designed experiments to characterize the mechanical behavior of a coaxial cable subject to cyclic multiaxial loadings. Combined torsional and tensile loads were applied in these tests to investigate the effect of pretorsion on the tensile behavior.

The accuracy of any analytical or computational model used to simulate the mechanical behavior of wire harnesses is highly dependent on the material properties used in the model. Unlike conventional structural materials, there is limited information on the mechanical properties of electrical wires and their constituents such as the polymeric insulation and the conductive core. Only a limited number of prior works (e.g., [25]) have attempted to experimentally characterize the material properties of constituents of commercial electrical wires. However, the softness of the insulation and the small diameter of the conductive core of most wires (often < 1 mm) impose significant challenges for separating these phases and characterizing their mechanical behavior via experimental testing. Further, since the major loading sustained by electrical wires during the assembly process is bending, the deformation response is highly influenced by the internal structure of the wire (e.g., the number and configuration of the strands in the conductive core). Thus, tension tests would not be useful to evaluate the effective properties of a wire in bending. Due to such challenges, although existing digital manufacturing software packages provide the desired computational efficacy, they lack the predictive capability to accurately simulate the assembly of wire harnesses for industrial applications.

In this work, we present a hierarchical approach involving analytical, computational, and experimental elements to characterize the mechanical behavior of single electrical wires and taped wire bundles. We show that incorporating the plastic deformation of wires in the reduced-order FE model is crucial to the accurate prediction of their deformed shapes. An optimization-based algorithm is introduced to evaluate the effective elastoplastic properties of wires based on experimental data obtained from customized bending tests. A high-fidelity 3D FE model is also developed to be used as a substitute for physical testing to evaluate the effective mechanical properties of wire bundles. This model relies on an explicit dynamic time integration scheme [26] and takes into account different sources of geometrical and material nonlinearities, including the elastoplastic behavior of wires, contact-friction between them, and the cohesive bonding between the tape and wires. We will show that upon proper evaluation of homogenized material properties in bending, a 1D FE model relying on beam elements can accurately predict the deformed shape of taped wire bundles.

The remainder of this article is structured as follows: In Section 2, we study the appropriate FE model for simulating the mechanical behavior of single electrical wires by comparing 1D and 3D models, as well as studying the effects of elastic and elastoplastic material behaviors. We also investigate the impact of residual stresses on the deformation responses of wires in that section. Section 3 presents a customized cantilever bending test for characterizing the force-deflection response of wires and their deformed shapes using a motion capture system. An optimization-based algorithm is introduced in Section 4 to calibrate the effective elastoplastic properties based on a set of experimental data, which is then validated with a different set of data. A high-fidelity 3D FE model of taped wire bundles, together with the required calibration and validation studies, is presented in Section 5. Final concluding remarks are provided in Section 6.

2. Appropriate mechanical model

Most software packages currently used for the digital manufacturing of wire harnesses rely on 1D elastic beam models, which often cannot accurately predict their deformed response. We postulate that the inaccuracy of existing harness simulations is primarily due to neglecting the nonlinear material behavior of wires (e.g., plasticity) rather than the use of a reduced-order model. To investigate this, we simulate the deformation response of a single electrical wire as the building block of wire harnesses. As shown in Fig. 2, an electrical wire is composed of a conductive core (e.g., multiple strands of annealed copper) wrapped in a polymer insulator such as polyvinyl chloride (PVC). Note that the mechanical properties of copper and PVC are highly dependent on the manufacturing process and can have large variations between different types of wires. To obtain realistic elastoplastic properties for these constituents in the current study, we employ the experimentally measured stress-strain responses of the copper and PVC used in an 8 AWG wire, as reported in [25,27]. These stress-strain responses are quantified by separating the PVC insulation from the copper core and performing tensile tests on each phase independently. Table 1 summarizes the resulting elastoplastic properties after calibration with the experimental data provided in [25,27], including the Young's modulus E, Poisson's ratio ν, yield stress σ_Y, strength coefficient K, and the strain hardening exponent n. Next, we briefly describe the governing equations used for evaluating these parameters.

Table 1
Mechanical properties of annealed copper and PVC reported in [25,27].

Material	E (MPa)	ν	σ_Y (MPa)	K (MPa)	n
Copper	67,908	0.35	182	353	0.54
PVC	115	0.42	2	21	0.23

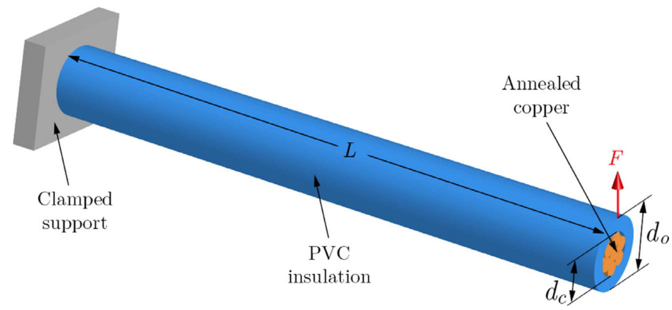

Fig. 2. Schematic of a cantilevered electrical wire composed of an annealed copper core and a PVC insulator, which is subject to a follower force at the free end.

2.1. Governing equations

The relationship between the Cauchy stress tensor $\boldsymbol{\sigma}$ and the total strain tensor $\boldsymbol{\varepsilon}$ in an elastoplastic material can be written as [28]

$$\boldsymbol{\sigma} = \mathbb{C} : (\boldsymbol{\varepsilon} - \boldsymbol{\varepsilon}^p), \tag{1}$$

where $\mathbb{C}$ is the fourth-order elasticity tensor and $\boldsymbol{\varepsilon}^p$ is the plastic strain tensor. For an isotropic material, $\mathbb{C}$ is characterized by two constants: the Young's modulus E and the Poisson's ratio ν. In order to evaluate the yield stress σ_Y, we employ the von Mises yield criterion (J_2 flow theory), in which the evolution of stress after the yield point can be described using a power law given by Khan and Huang [29], Jirásek and Bazant [30].

$$\bar{\sigma} = \sigma_Y + K(\bar{\varepsilon}^p)^n \quad \text{if } \bar{\sigma} \geq \sigma_Y, \tag{2}$$

In the equation above, $\bar{\sigma}$ is the effective stress and $\bar{\varepsilon}^p$ is the effective plastic strain $\bar{\varepsilon}^p$, which is the cumulative measure of plastic strain increments. K and n are referred to as the strength coefficient and the strain hardening exponent, respectively. The effective stress $\bar{\sigma}$ can be evaluated as [28]

$$\bar{\sigma} = \left(\tfrac{3}{2}\mathbf{s} : \mathbf{s}\right)^{\frac{1}{2}} = \sqrt{\tfrac{1}{2}\left[(\sigma_1 - \sigma_2)^2 + (\sigma_2 - \sigma_3)^2 + (\sigma_3 - \sigma_1)^2\right]}, \tag{3}$$

where $\mathbf{s} = \boldsymbol{\sigma} - p\mathbf{I}$ is the deviatoric stress tensor, $\mathbf{I}$ is the identity tensor, p is the spherical (hydrostatic) stress, and σ_i denotes the ith principal stress. Also, the effective plastic strain $\bar{\varepsilon}^p$ can be written as

$$\bar{\varepsilon}^p = \int \mathrm{d}\bar{\varepsilon}^p, \tag{4}$$

where $\mathrm{d}\bar{\varepsilon}^p$ is the effective plastic strain increment. In the J_2 flow theory, $\mathrm{d}\bar{\varepsilon}^p$ is evaluated as

$$\mathrm{d}\bar{\varepsilon}^p = \left(\tfrac{2}{3}\mathrm{d}\boldsymbol{\varepsilon}^p : \mathrm{d}\boldsymbol{\varepsilon}^p\right)^{0.5} = \sqrt{\tfrac{2}{3}\left(\mathrm{d}\varepsilon_1^p + \mathrm{d}\varepsilon_1^p + \mathrm{d}\varepsilon_3^p\right)}, \tag{5}$$

where $\mathrm{d}\boldsymbol{\varepsilon}^p$ is the plastic strain increment tensor and $\mathrm{d}\varepsilon_i^p$ is the ith principal plastic strain increment.

In a reduced-order 1D isotropic beam model of an electrical wire, assuming that $\sigma_1 = \sigma$, $\varepsilon_1 = \varepsilon$, and $\varepsilon_1^p = \varepsilon^p$, the strain hardening equation given in (2) reduces to

$$\sigma = \sigma_Y + K(\varepsilon^p)^n, \quad \text{if } \sigma \geq \sigma_Y. \tag{6}$$

After evaluating E and σ_Y, values of n and K can be calibrated with an experimentally derived $\sigma - \varepsilon$ curve as

$$n = \frac{\mathrm{d}\ln(\sigma - \sigma_Y)}{\mathrm{d}\ln(\varepsilon^p)}, \quad K = \frac{\sigma - \sigma_Y}{(\varepsilon^p)^n}. \tag{7}$$

2.2. 3D versus 1D FE models

In the current manuscript, FE is employed to simulate the mechanical behavior of electrical wires, as this method is well established in industry and being used in several digital manufacturing software packages. Here, we compare the performance of 1D and 3D FE models of a cantilevered 8 American wire gauge (AWG) wire with a length of $L = 10$ cm, conductor (copper core) diameter of $d_c = 3.26$ mm, and the outer diameter of $d_o = 4.86$ mm (Fig. 2). Similar to existing digital manufacturing software packages, we temporarily overlook the elastoplastic behavior of the copper core and PVC insulation, assuming that both components have a linear elastic behavior. Note that the FE simulations take into account the geometrical nonlinearity emanating from large deformation of the wire due to applying a follower force of $F = 24$ N (i.e., a force that remains perpendicular to the wire) to the free end of the cantilever.

As shown in Fig. 3a, the conforming mesh created for the 3D FE model is composed of 20-node hexahedral (brick) elements. We have also employed selective reduced integration [31] for assembling the stiffness matrix to facilitate convergence and avoid shear locking. To investigate the effect of interfacial bonding between the copper core and the PVC insulation on the deformed shape, two FE models assuming (i) perfect bonding and (ii) contact-friction between them are constructed (friction coefficient: $\mu = 0.1$). Note that the first assumption is closer to reality, since no adhesive is applied along the copper-PVC interface during the fabrication of electrical wires. However, as shown in Fig. 4, both models yield nearly identical deformed shapes, indicating that a perfectly bonded copper-PVC interface assumption has a negligible impact on the 3D FE simulation results.

To compare the deformed shape of the wire obtained from the 3D FE simulation with a reduced-order 1D model, we used 50 second-order beam (Hermitian) elements to discretize the wire. The diameter of the homogenized wire is assumed to be $d = d_o = 4.86$ mm and its effective Young's modulus is evaluated as $E_{\text{eff}} = 13.84$ GPa. This homogenized value is obtained using the flexural rule of mixtures [32], which can be expressed as

$$(EI)_{\text{eff}} = (EI)_{\text{PVC}} + (EI)_{\text{Cu}}, \tag{8}$$

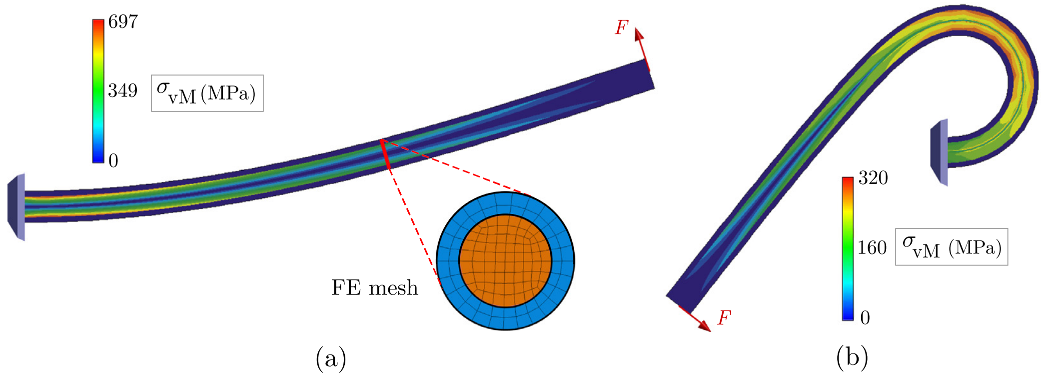

Fig. 3. 3D FE simulation of the deformed shape and von Mises stress field in the cantilevered wire subject to a follower force of $F = 24$ N using: (a) elastic material model, where σ_{vM} exceeds the yield stress values of copper and PVC given in Table 1; (b) elastoplastic material model, which realistically predicts the deformed shape.

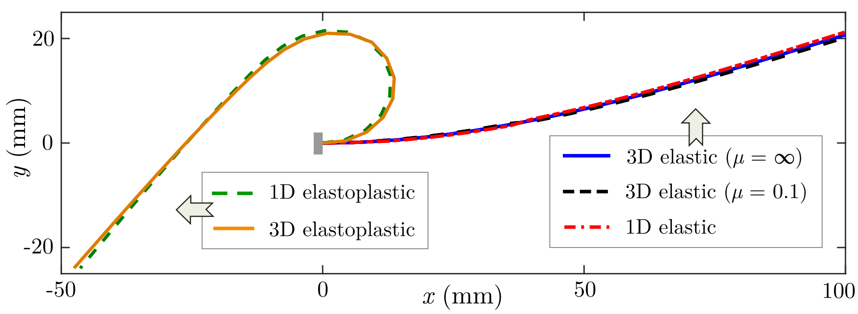

Fig. 4. Comparison between 1D and 3D FE simulations of the deformed shapes of the cantilevered beam shown in Fig. 2 subject to a follower force $F = 24$ N considering elastic (right) and elastoplastic (left) material models. The clamped end of the wire is located at (0, 0).

where I is the second moment of area ($I_{\mathrm{eff}} = \frac{\pi}{64} d^4$). Similarly, the effective Poisson's ratio $\nu_{\mathrm{eff}} = 0.39$ of the homogenized wire is evaluated as

$$(\nu A)_{\mathrm{eff}} = (\nu A)_{\mathrm{PVC}} + (\nu A)_{\mathrm{Cu}}, \tag{9}$$

where A is the cross sectional area. A comparison between the resulting 1D FE prediction of the deformed shape of the cantilevered wire with the 3D simulations is provided in Fig. 4, showing a negligible difference between the results. Note that the computational cost associated with the 1D model is less than 2% of that corresponding to the 3D simulation relying on the assumption of a perfectly bonded copper-PVC interface.

2.3. Elastic versus elastoplastic material models

The study above indicates that a 1D FE model relying on effective material properties evaluated using the rule of mixtures can accurately predict the deformed shape of an electrical wire provided that the wire constituents maintain a linear elastic behavior. However, as shown in Fig. 3a, the maximum von Mises stress σ_{vM} predicted by the 3D FE simulation in the copper core of the cantilevered wire is approximately 3.8 times larger than its yield stress ($\sigma_{\mathrm{vM}}^{\max} = 697$ MPa, $\sigma_Y = 182$ MPa). In other words, despite the relatively small deflection of this cantilevered wire, the linear elastic assumption is already violated and neither the 3D nor the 1D FE model simulates the actual physical behavior of the wire. Thus, a realistic simulation of the deformation response of the wire requires incorporating the elastoplastic constitutive behaviors of the copper and PVC in the model.

In order to quantify the impact of nonlinear material behavior of the wire on its deformation response, we repeated the 3D FE simulation using an elastoplastic material model with the properties given in Table 1. The resulting deformed shape of the wire, together with the von Mises stress distribution across its longitudinal section, is depicted in Fig. 3b. Note the significant difference between this simulation and the bent shape of the wires predicted by the linear elastic model (Fig. 3a). This large discrepancy between the results of elastic and elastoplastic models is better visualized in Fig. 4. This figure also provides a comparison between the 1D and 3D elastoplastic FE simulations of the bent shape of the wire, showing that the reduced-order 1D model can closely replicate the 3D FE result. The nonlinear material properties used in this 1D model include $(\sigma_Y)_{\mathrm{eff}} = 59.5$ MPa, $K_{\mathrm{eff}} = 136$ MPa, and $n_{\mathrm{eff}} = 0.88$. It must be noted that when the plastic deformation begins, the rule of mixtures is no longer valid for evaluating the effective elastoplastic properties of the wire. Thus, the effective properties above are obtained using an optimization-based algorithm, which will be described in detail in Section 4.

The discrepancy between the elastic and elastoplastic simulations on one hand and the similarity of 1D and 3D simulations for both cases on the other hand confirms the postulate proposed at the beginning of this section. In other words, a 1D FE model relying on beam elements would be adequate for the accurate prediction of the deformed shape of an electrical wire provided that its elastoplastic material behavior is taken into account. This observation reassures that the lack of predictive capability of digital manufacturing software packages is not due to using geometrically reduced-order 1D beam elements, but instead emanates from adopting an oversimplified constitutive model (linear elastic).

2.4. Effect of residual stresses

Given the importance of plasticity on the deformed shape of electrical wires, it is also worthwhile to investigate the effect of residual stresses on their mechanical behavior. Several experimental or numerical methods can be used to quantify the residual stresses developed in materials during the manufacturing processes [33,34]. However, electrical wires are not designed for structural performance and could be subject to various un-quantified mechanical loads during the manufacturing, shipping, and handling before the assembly. While it would be

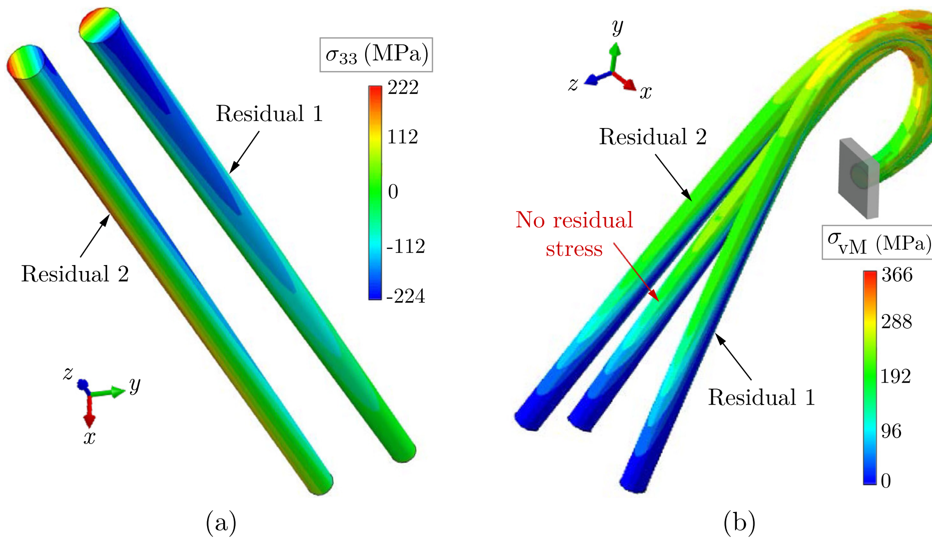

Fig. 5. (a) Two different distributions of residual stresses in the copper core of the cantilevered wire with σ_Y = 182 MPa; (b) comparison between deformed shapes and von Mises stress fields in wires with and without residual stresses subject to a follower force of $F = 24$ N.

practically impossible to characterize the residual stresses developed in wires due to their loading histories, the non-straight shapes of wire harness branches indicate the presence of residual stresses when a wire is forced into a straight position. Thus, understanding the effect of residual stresses on bending characteristics could shed light on the variability expected in both the mechanical testing and FE simulation of the mechanical behavior of wires.

Here, we compare the deformation response of the cantilever wire studied in the preceding section under a no residual stress condition with two simulations considering the presence of residual stresses in the copper core, as depicted in Fig. 5a. In order to obtain a realistic distribution of residual stresses in these cases, the wires are pre-loaded in the 3D FE models and loading and unloading processes are simulated to evaluate the residual stresses. For the case labeled Residual 1 (Fig. 5a), a non-follower force of $F = 5\mathbf{e}_1 + 5\mathbf{e}_2 + 5\mathbf{e}_3$ N is applied at the free end of the cantilever, followed by a moment of $\mathbf{M} = 0.2\mathbf{e}_1 + 0.2\mathbf{e}_2 + 0.2\mathbf{e}_3$ N.m. The residual stress labeled as Residual 2 is obtained by first applying a vertical force of $F = 3\mathbf{e}_1 + 3\mathbf{e}_2 + 3\mathbf{e}_3$ N, followed by a moment of $\mathbf{M} = 0.5\mathbf{e}_1 + 0.5\mathbf{e}_2 + 0.5\mathbf{e}_3$ N.m.

Fig. 5b illustrates the FE simulations of deformed shapes of the cantilevered wires with and without residual stress subject to a follower force of $F = 24$ N, together with the predicted von Mises stress field in the copper core of each wire. These simulations show a notable difference between the deformed shapes of the wires depending on the initial distribution of residual stresses. Since it would not be practical to quantify residual stresses in actual electrical wires, one could anticipate a potential variability in results of mechanical tests on multiple wire samples, as well as an inevitable uncertainty in the predictive capability of elastoplastic FE simulations.

3. Experimental characterization

3.1. Challenges and required considerations

One of the major challenges toward the construction of reliable 1D FE models of electrical wires and wire harnesses is to accurately evaluate their effective elastoplastic properties. Since most wires used for automotive applications are merely designed based on the target electrical performance (e.g., conductor resistance, insulation breakdown voltage, and temperature rating), mechanical properties of their constituents are largely unexplored and often not provided by the manufacturer. Also, between different electrical wires used in a vehicle, there could be a significant variation in the mechanical behavior of the conductive core and the insulation, where the latter could have different chemical compositions. Similarly, the conductive core could be made of aluminum or copper and have a stranded (Fig. 2) or solid architecture. For standard conductors, there could be different strand diameters and numbers of strands, as well as different helical twist angles and with circular or compressed cross-sectional shapes. Such features could lead to large differences between the effective elastoplastic properties of wires subject to bending loads, which is the dominant loading sustained during the assembly process. Moreover, given the small diameter of the conductor and the small thickness of the soft insulation, separating these phases without damaging their materials and structures to perform the tests needed to characterize their mechanical behavior would be a challenging task.

Given the challenges outlined above, it would be more practical to experimentally measure the effective elastoplastic properties of an electrical wire by testing it as a whole. However, even for wires with solid conductive cores, a tensile test would not characterize the effective nonlinear material properties needed to simulate its bending response. Studying the evolution of the normal stress σ in the cross section of a wire subject to a tensile force (Fig. 6a) and a pure bending moment (Fig. 6b) could better elucidate this issue. In the former case, the stress profile is approximately uniform in the conductor and insulator but not equal between the two materials, both before and after the yield point. On the other hand, as shown in Fig. 6b, the normal stress in the wire subject to pure bending has a linear distribution in each phase in the elastic zone. As the bending moment increases, the plastic behavior initiates at the farthest regions of each phase from the neutral axis and then evolves toward it, leading to a complex stress profile in the wire. Such distinct stress profiles in an electrical wire subject to uniform tension and pure bending would lead to different homogenized elastoplastic properties. Thus, the effective properties required to simulate the deformed shape of a wire subject to bending moments must be calibrated with experimental data obtained from bending tests. In the current work, a cantilever bending test was selected over a three-point bending test due to the ability to realistically simulate the clamped boundary condition (compared to roller supports in the latter) for wires with small diameters (< 1 mm).

3.2. Sample preparation

Samples of single wires for cantilever bending tests were prepared by cutting pieces of wire off a spool and gently straightening them. Re-

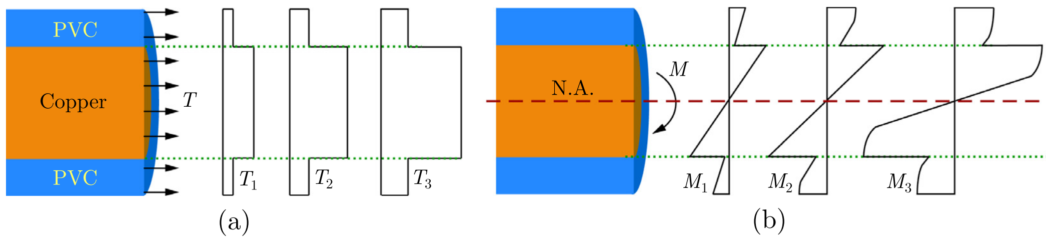

Fig. 6. Evolution of the elastoplastic normal stress profile in an electrical wire subject to (a) uniform tension ($T_3 > T_2 > T_1$); (b) pure bending ($M_3 > M_2 > M_1$).

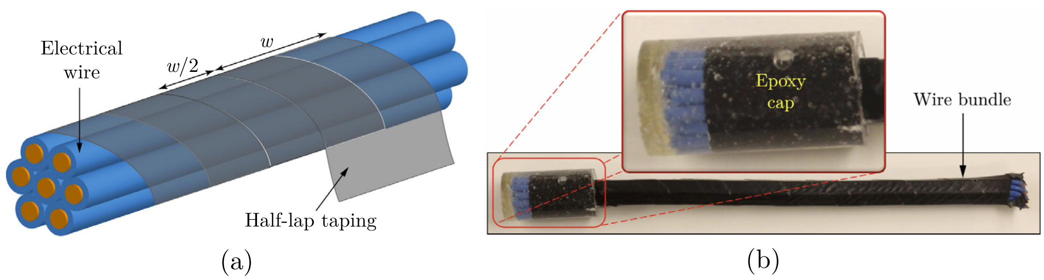

Fig. 7. (a) Schematic of a half-lap taped wire bundle; (b) cantilevered taped wire bundle with an epoxy cap, which is used to constrain all the degrees of freedom at the fixed end.

Table 2
Conductor diameters (d_c), outer diameters (d_o), and densities (ρ) of three types of electrical wires used in the cantilever bending tests.

Wire type	1	2	3
d_c (mm)	0.7	0.85	1.0
d_o (mm)	1.1	1.25	1.4
ρ (g/cm^3)	4.06	4.31	4.97

flective tape markers were then placed along the length of the samples to characterize the deformed shape of wires during experiments using a motion capture system. Samples of three types of electrical wires with stranded annealed copper cores and PVC insulation were prepared. The inner and outer diameters, as well as densities of these wires are reported in Table 2. The conductor cores of these wire types are composed of compressed strands, the numbers and diameters of which are different. Samples with lengths of $L_1 = 85$ mm (for all wires) and $L_2 = 100$ mm (for wire types 1–3) were prepared. In Section 4, the experimental data obtained from the cantilever bending tests conducted on shorter samples will be used to calibrate the effective elastoplastic properties, while the results of tests on longer samples will be employed to validate the 1D FE model.

Multiple samples of taped wire bundles are also prepared to characterize their mechanical behavior as one of the main components of wire harnesses. As shown in Fig. 7a, wires in each bundle are packed together using a helical half-lap taping with the width w. Half of the width of the tape in each helix overlaps with the previous helix, resulting in a taping with twice the thickness of each layer of the tape. It must be noted that tension tests are separately conducted on the tape samples to quantify their elastoplastic properties. For the cantilever bending test of taped wire bundles, wire types 2 and 3 are used to build bundles of 7, 12, and 19 wires, as well as a mixed bundle of 10 wires of type 2 and 9 wires of type 3. The lengths of samples vary based on the number of wires to control the total bending stiffness based on the capacity of the load cell. Fig. 7b shows one of the taped bundle samples, where the left end is cast in a polycarbonate tube filled with epoxy. This epoxy cap is used to firmly grip the fixed end of the bundle using a custom-made adapter mounted on the load frame's shaft to avoid applying direct pressure on the wires. This provides a boundary condition that is close to the case of an ideally clamped end for the cantilever bending test.

3.3. Experimental setup

A general overview of the experimental setup is depicted in Fig. 8a. The sample is secured in a polycarbonate fixture at one end with screws to ensure a zero slope clamped boundary condition. To prevent lateral forces and maintain an approximately vertical load during the cantilever wire bending, an aramid strand is used to attach the free end of the wire to a load cell located 760 mm above the sample. The aramid strand can be assumed to be inextensible due to its high tensile stiffness compared to the bending stiffness of electrical wires. For the single wire bending test, a 20 g Cooper™ LS 270 load cell is used, whereas for the wire bundle bending test, a 2 lb Futek™ LSB200 S-beam load cell is employed. The polycarbonate fixture securing the clamped end is mounted on a rod connected to a stepper motor. Note that deformations of the sample make it difficult to deflect the free end of the cantilever wire while simultaneously measuring the load. Thus, the stepper motor is employed to displace the clamped end, while the force applied by the aramid strand is recorded using a load cell (Fig. 8b). The speed and direction of the stepper motor rotation is controlled by a dSPACE™ 1103 controller, which also receives input from the load cell through a signal conditioner to record the measured force.

One disadvantage of using a stepper motor is the lack of feedback during the test to identify potential missing steps. Therefore, one cannot assume that the displacement corresponds to the number of steps commanded. In order to address this challenge and also to accurately capture the deformed shape of the sample throughout the test, an Optitrack™ Flex 13 motion capture system is used. The motion capture system consists of four cameras that are positioned such that at least two cameras can view all the reflective markers throughout the experiment. Each camera has 28 IR LEDs and an IR sensor. The system measures the 3D position of the markers based on the triangulation of images from multiple cameras. The shape of the deformed wire is then quantified based on the spatial coordinates of each marker recorded by the motion capture system. In order to prohibit shiny surfaces from interfering with the motion capture system, they are covered with a blue colored masking tape, as shown in Fig. 8.

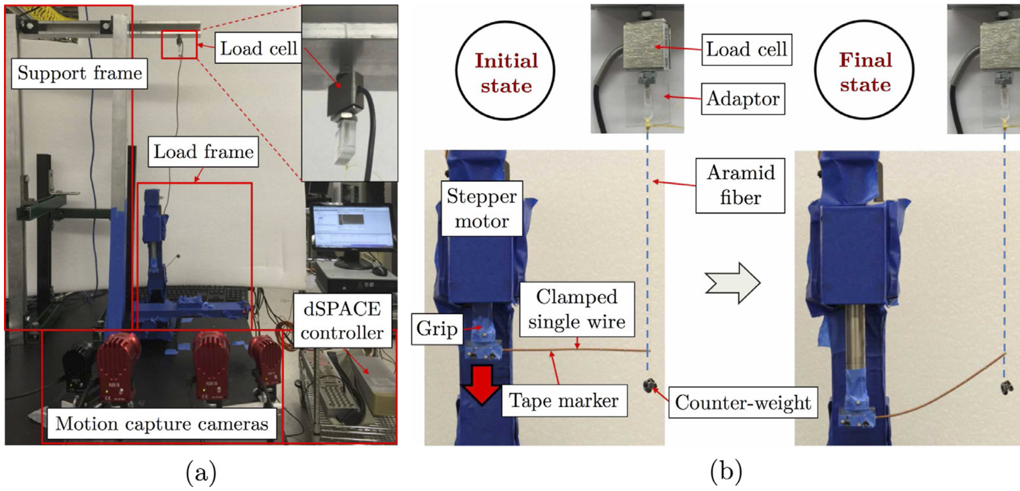

Fig. 8. (a) Cantilever bending test setup for single wires and taped wire bundles; (b) initial and deformed shapes of a wire sample.

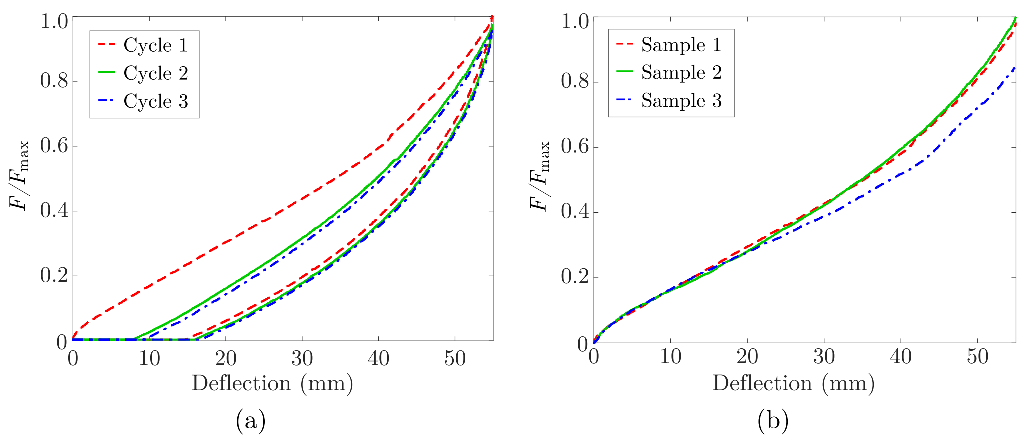

Fig. 9. Experimentally measured force-deflection responses of cantilevered wire samples of type 1 with $L = 85$ mm: (a) cyclic responses of sample 1; (b) loading responses of three different samples.

3.4. Testing procedure and experimental results

The cantilever bending test is conducted by deflecting the sample at a rate of 1 mm/s for approximately 53 mm, followed by unloading at the same rate to quantify the plastic deformation. As the sample undergoes bending, the vertical force applied at the free end using the aramid string is measured with a load cell. Simultaneously, the motion capture system records the position of all seven markers at 120 frames per second. As shown in Fig. 8b, a small counterweight of 2.7 g is hung at the free end of the sample throughout the test to maintain the tension in the aramid string. Three samples of each type of wire or taped wire bundle are tested, and the loading-unloading process is repeated for three cycles in each test to characterize the effects of cyclic loading on the deformation response.

Fig. 9a shows the experimentally measured cyclic force-deflection responses of sample 1 of wire type 1 ($L = 85$ mm) at the free end of the cantilevered wire. Note that in each force-deflection plots presented in this work, force values are normalized by the maximum force $F_{\max}$ in that plot. The loading responses of three different samples of this type of wire are depicted in Fig. 9b. The initial nonlinearity in the force-deflection responses is due to the complex internal architecture of the wires, as well as the fact that their initial shapes are not perfectly straight. The nonlinearity at higher deflections is due to the nonlinear material behavior of the wire constituents, which is shown by the cyclic results in Fig. 9a. Note that according to the study presented in Section 2.4, one of the reasons for the difference observed in the force-deflection response

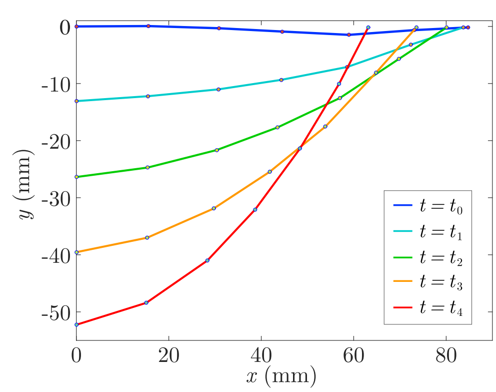

Fig. 10. Deformed shapes of sample 1 of wire type 1 ($L = 85$ mm) recorded by a motion capture system during the cantilever bending test.

of sample 3 compared to the other two samples in Fig. 9b could be differences in residual stresses between the wire samples. Five snapshots of the deformed shape of sample 1 of wire type 1, which are recorded by the motion capture system during the cantilever bending test, are illustrated in Fig. 10. Note that since the wire is highly flexible and has been manually straightened, the initial shape of the sample shown in this figure is not perfectly linear.

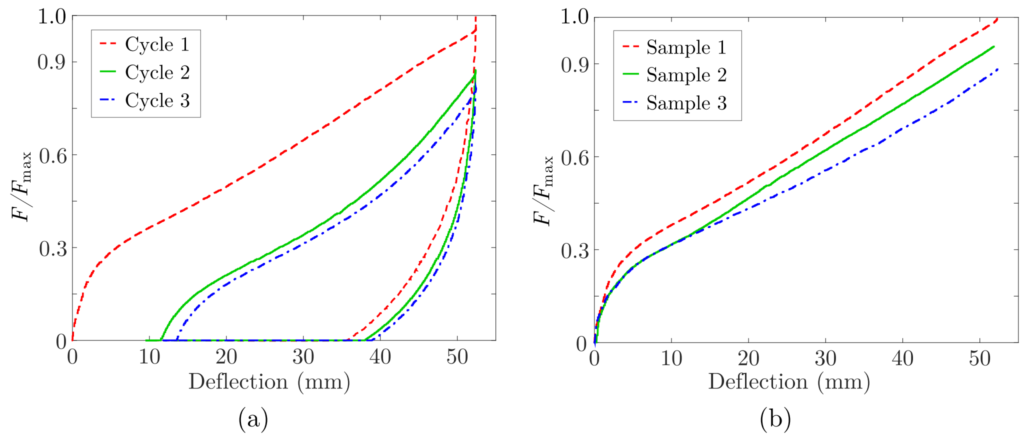

Fig. 11. Experimental force-deflection responses of cantilevered taped wire bundle samples composed of 7 wires of type 2 with $L = 114$ mm: (a) cyclic responses of sample 1; (b) loading responses of three different samples.

Fig. 11($L = 114$ mm) illustrates the force-deflection output for 7-wire bundles of wire type 2. As expected, the cyclic results depicted in Fig. 11a show a significant plastic deformation in the taped wire bundle after the first loading/unloading cycle. Further, as illustrated in Fig. 11b, a higher variability is observed in the force-deflection responses of the bundle samples compared to the single wire results shown in Fig. 9b. In addition to the variability of individual wires, this larger cumulative range of responses may also be due to the variability in how the wires are manually packed and taped together to form the bundles during the manufacturing process. The experimental force-deflection responses of other single wire and wire bundle samples will be presented in Sections 4 and 5, which are used for the calibration and validation of FE models.

4. Effective properties of single wires

4.1. Calibration of the elastoplastic model

The average force-deflection responses obtained from the cantilever bending tests of single wire samples are used to determine the effective elastoplastic properties of each type of wire. After calibrating E and σ_Y with the experimental data, the resulting values are employed to determine the effective K and n using an optimization-based approach. Note that since there is no standard for defining the elastic zone of an electrical wire, the yield point can be defined as the first point that the experimental force-deflection curve deviates from the response of a corresponding FE simulation with linear elastic properties, while taking into account the geometric nonlinearity. Although assuming a larger elastic zone would increase the error in predicting the deformed shape of a wire, it has the advantage of reducing the computational cost by maintaining the elastic behavior over a wider range of deformation. A parametric study on the tradeoff between different assumptions for the yield point showed that assuming that wires maintain a linear elastic behavior up to a tip deflection equal to 5% of their lengths during cantilever bending tests is the best choice.

In order to evaluate the effective elastoplastic properties of a wire, the elastic beam theory [35] is first employed to relate E to the experimentally measured force F and the tip deflection δ in the elastic zone. Using the tip deflection $\delta_{5\%} = 5\%L$ to quantify the elastic zone, the effective modulus of elasticity of the wire can be evaluated as

$$E = \frac{F_{5\%}L^3}{3\delta_{5\%}I} = \frac{1280F_{5\%}L^2}{3\pi d_o^4}, \tag{10}$$

where $F_{5\%}$ is the applied force corresponding to $\delta_{5\%}$. The maximum normal elastic stress in the cross section of the cantilevered wire is then induced by the maximum bending moment, $M = FL$, which occurs at the fixed end of the wire. We determine σ_Y as the maximum normal stress caused by the bending moment corresponding to $\delta_{5\%}$ (i.e., $M_{5\%} = F_{5\%}L$), which can be written as

$$\sigma_Y = \frac{32F_{5\%}L}{\pi d^3}. \tag{11}$$

Then, we implement an optimization algorithm to characterize the effective strength coefficient K and strain hardening exponent n of the wire introduced in power law equation (6). As initial estimates for these parameters, the Holloman's (Ludwik's) equation [36,37] is employed to approximate the stress-strain curve after the yield point as

$$\sigma = K\varepsilon^n, \quad \text{if } \sigma \geq \sigma_Y. \tag{12}$$

This estimate can be obtained by rewriting the stress-strain relationship at the yield point as $\sigma_Y = K(\frac{\sigma_Y}{E})^n$, given the continuity of the $\sigma - \varepsilon$ curve at the yield point. By solving this relation for K, and substituting it in (12), we can rewrite the Holloman's equation as

$$\sigma = \sigma_Y\left(\frac{E\varepsilon}{\sigma_Y}\right)^n \quad \text{if } \sigma > \sigma_Y. \tag{13}$$

In order to estimate n, we first employ (13) to evaluate the tangent modulus $E_t = \frac{d\sigma}{d\varepsilon}$ in the plastic zone as

$$E_t = nE\left(\frac{\sigma}{\sigma_Y}\right)^{\left(1-\frac{1}{n}\right)}. \tag{14}$$

to obtain an initial estimate for $E_{t,\,Y}$, the experimental force-deflection curve is converted to a stress-strain curve using $\sigma = \frac{Md_o}{2I} = \frac{32FL}{\pi d_o^3}$ over a small range of ε after the yield point. This is an approximation of the right slope of the $\sigma - \varepsilon$ curve at this point (i.e., the slope after the yield point), which yields the following initial estimate for n

$$n_0 = \frac{E_{t,Y}}{E}. \tag{15}$$

A first estimate for the effective strength coefficient is then evaluated as

$$K_0 = \frac{E^n}{\sigma_Y^{n-1}}. \tag{16}$$

To more accurately evaluate the initial estimates obtained from (15) and (16), we adopt the Nelder-Mead simplex optimization algorithm [38,39]. The algorithm determines the optimal values of K and n that minimize the L_2-norm of the error E_{L_2} corresponding to the simulated and experimental force-deflection responses of each cantilever wire. The relative L_2-norm of the error can be computed as

$$E_{L_2} = \left(\int_0^{\delta_{\max}} \left[F_{\exp}(\delta) - F_{\mathrm{FE}}(\delta)\right]^2 \mathrm{d}\delta\right)^{\frac{1}{2}}, \tag{17}$$

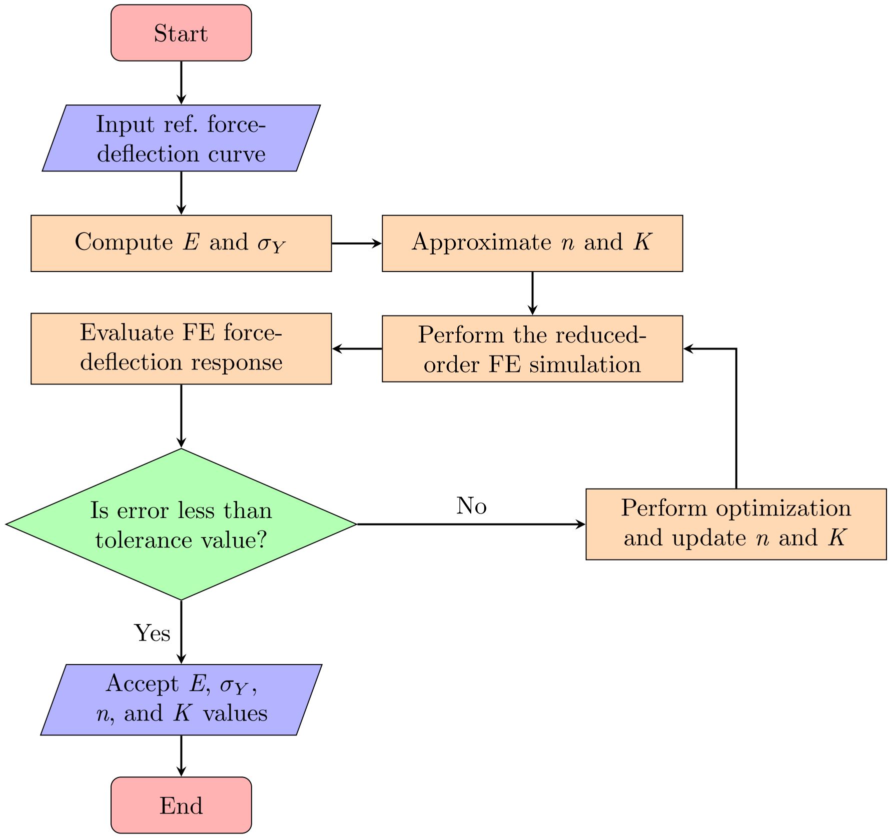

Fig. 12. Flow chart describing the process of calibrating the FE model with reference force-deflection curves, which can be either experimental or high-fidelity FE results.

where δ_{max} is the maximum deflection, and F_{exp} and F_{FE} are forces obtained from the experiment and the simulation, respectively. The FE analyses for approximating F_{FE} are conducted using a wire model that is discretized with 50 second-order 1D beam elements.

The Nelder-Mead optimization is conducted by building a non-degenerate triangular simplex with vertices $[K_0, n_0]$, $[1.05K_0, n_0]$, and $[K_0, 1.05n_0]$ as the first step. In an iterative process, after evaluating E_{L_2} corresponding to each vertex, the vertex with the largest error is replaced with a better estimate using the transformation operators (reflection, expansion, contraction, etc.) applied on the simplex. In each iteration, the optimization code automatically executes the FE solver and recomputes the force-deflection response to update E_{L_2}. This iterative process stops when the size of the working simplex becomes excessively small or E_{L_2} converges to the user-defined tolerance value. Note that the former stop criterion leads to a premature convergence, i.e., not being able to find the optimal values of K and n due to the inability to further evolve the vertices of the simplex. Therefore, although the Nelder-Mead technique is a computationally efficient, straightforward optimization algorithm, avoiding a premature convergence with this method is contingent upon using appropriate initial estimates for K and n. To achieve this, rather than randomly selecting K_0 and n_0, it is essential to implement (13) and (15) to obtain proper initial estimates for each variable. The flow chart summarizing the entire process of calibrating the FE model with reference force-deflection results is presented in Fig. 12. This reference data can be obtained either from experimental tests or high-fidelity FE simulations.

4.2. Calibration and validation results

Using the optimization-based algorithm described in Section 4.1, 1D FE models of single wires are calibrated against cantilever bending test data for short wire samples ($L = 85$ mm) to determine the effective material properties. Note that the weight of the wires, evaluated based on the experimentally measured density values reported in Table 2, are considered in these models. The resulting effective elastoplastic properties of the wire types 1–3 are reported in Table 3. A parametric study showed that using different values for the effective Poisson's ratio of wires has a negligible impact on the resulting bending force-deflection response. Thus, we use $\nu_{eff} = 0.39$ for all wire types, which is the average of the value evaluated using the rule of mixtures (9) for each wire. Fig. 13 shows that there is a good agreement between the simulated and average experimental force-deflection responses of these wires. Similarity between the deformed shapes predicted by the 1D FE simulation and measured using the motion capture system is confirmed in the inset of Fig. 13 for wire type 1. Therefore, in addition to matching the force-deflection responses, the calibrated FE model can properly replicate the deformed shapes of the wires observed in the cantilever bending tests.

Table 3
Effective elastoplastic material properties of single wires after the calibration with experimental data.

Wire type	E (MPa)	σ_Y (MPa)	K (MPa)	n
1	5,021	3.90	3222	0.99
2	5,641	4.95	850	0.78
3	4,528	4.52	1,327	0.90

The deformation responses of cantilever wire types 1–3 with $L = 100$ mm are simulated to validate the accuracy of the elastoplastic 1D FE models calibrated using the data from short wire samples (Table 3). As depicted in Fig. 14, the resulting force-deflection curves show a decent agreement with those obtained experimentally from bending tests on long wire samples. Fig. 15 illustrates the error curves associated with the

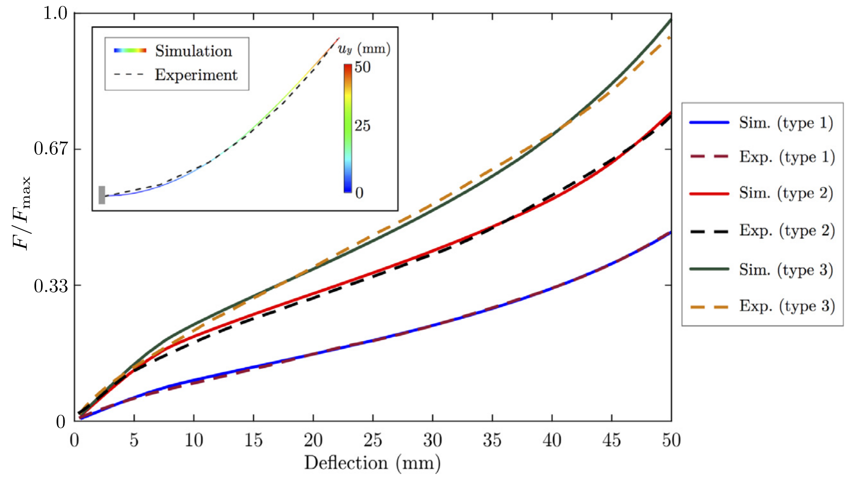

Fig. 13. Comparison between the average experimental and 1D FE simulated force-deflection responses of short wire samples (L = 85 mm) of types 1–3 after the calibration with experimental data. The inset of the Figure compares the bent shapes of wire type 1, predicted by the FE model and recorded using a motion capture system.

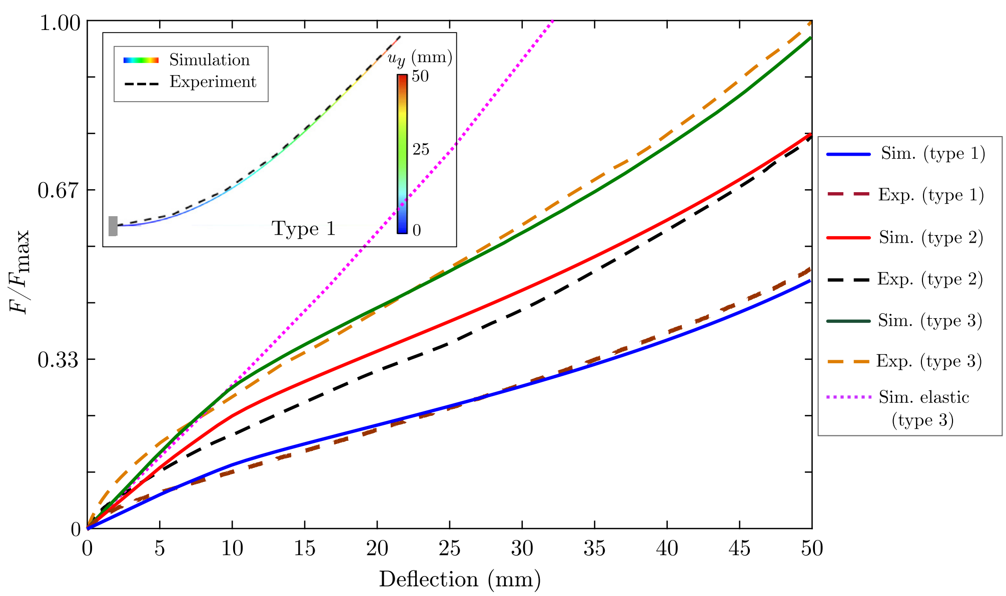

Fig. 14. Comparison between the average experimental and 1D FE simulated force-deflection responses of long wires (L = 100 mm) of types 1–3 for validating the model. The inset of the figure shows the bent shape of wire type 1 predicted by the FE simulation and recorded using a motion capture system.

average of experimental and 1D simulation results presented in Fig. 14, which are computed as

$$Err(\delta) = \left[F_{\exp}(\delta) - F_{\mathrm{FE}}(\delta)\right]/F_{\max}. \tag{18}$$

As shown in this figure, the values of error are within the bounds 5.1×10^{-2} and 5.7×10^{-2}. Note that the error values minimized during the optimization process are described in terms of L_2-norms of the error; therefore the actual error can be either positive or negative. For each error curve, the Root Mean Square (*RMS*) of the error is also reported, which is evaluated as

$$RMS = \left(\frac{1}{\delta_{\max}}\int_0^{\delta_{\max}} Err(\delta)^2 \mathrm{d}\delta\right)^{\frac{1}{2}}, \tag{19}$$

The *RMS* values vary between 1.26×10^{-2} and 3.65×10^{-2}, which is an acceptable range taking into account the previous cold working and non-straight initial shapes of wire samples, as well as the presence of residual stresses. Also, as shown in the inset of Fig. 14, the simulated bent shape of wire type 1 is approximately identical to that obtained from the motion capture system for this sample. To shed more light on the importance of considering the elastoplastic behavior of the wires in these simulation, the deformation response of wire type 3 is also simulated using a linear elastic model with the material properties given in Table 3. According to Fig. 14, the force-deflection curve corresponding to this simulation is considerably different than the experimental result, which reemphasizes the lack of predictive capability of linear elastic FE models.

5. Modeling taped wire bundles

The optimization-based calibration algorithm described in the preceding section can be employed to evaluate the effective properties of all single wires used in the fabrication of a wire harness based on experimental data (e.g., cantilever bending tests). However, it would not be practical to apply a similar approach to wire bundles, since the ex-

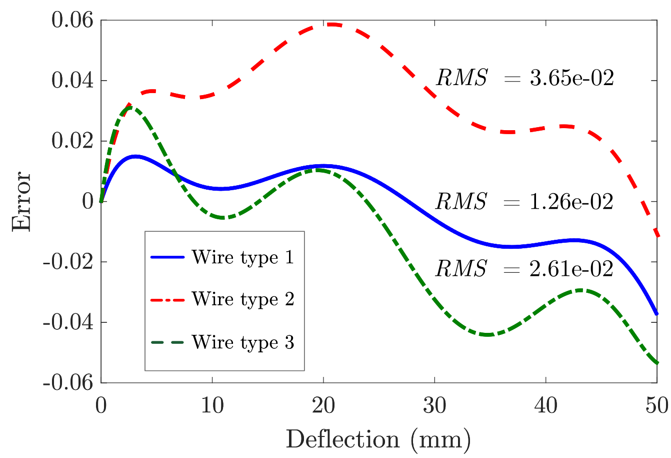

Fig. 15. Error curves betwee the average experimental and 1D FE simulated force-deflection responses shown in Fig. 14 for long wires (L = 100 mm) of types 1–3. *RMS* values for each curve are also reported.

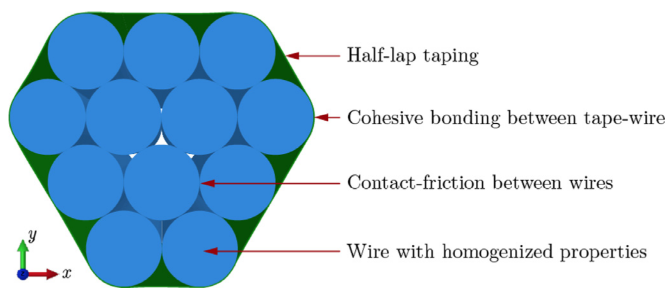

Fig. 16. Schematic of a taped wire bundle composed of 12 electrical wires.

perimental testing of hundreds or thousands of taped wire bundles with various combinations of electrical wires would be an extremely laborious and time consuming task. Thus, in this section we aim to develop a high-fidelity 3D FE model for taped wire bundles to serve as a surrogate for physical testing.

5.1. Developing 3D FE models

Fig. 16 illustrates the typical internal architecture of a taped wire bundle, composed of 12 wires packed together using a half-lap taping. To construct a high-fidelity FE model of the wire bundle, in addition to effective properties of individual wires, mechanical properties of the plastic tape are also needed. Experimental data from tensile tests conducted on single layers of the tape were converted into a true stress-strain curve, from which elastoplastic properties were evaluated as E_{tape} = 119 MPa, $(\sigma_Y)_{\text{tape}}$ = 2.4 MPa, K_{tape} = 16.3 MPa, and n_{tape} = 0.73.

A high-fidelity FE model of taped wire bundles must also consider contact friction shear and normal stresses between adjacent wires, as well as the cohesive bonding along tape-wire interfaces. The classical isotropic Coulomb friction model is used in this study to relate the normal and shear stresses across the wire interfaces. A constant friction coefficient μ can be used to simulate friction forces between wires in a static model. However, in a dynamic friction model, the friction coefficient varies between static μ_s (sticking condition) and kinetic μ_k coefficients (slipping condition), which can be simulated using an exponential decay function as [40]

$$\mu = \mu_k + (\mu_s - \mu_k)e^{-d_c\dot{\gamma}}. \tag{20}$$

where d_c is a user-defined decay coefficient and $\dot{\gamma} = \sqrt{\dot{\gamma}_1 + \dot{\gamma}_2}$ is the equivalent slip rate, where $\dot{\gamma}_1$ and $\dot{\gamma}_2$ are two slip velocities along the local tangent directions for the contact surface along the interface between adjacent wires.

The cohesive adhesion along tape-wires interfaces is characterized using a linear elastic traction-separation law (in the absence of damage), which can be written as [41]

$$\mathbf{t} = \begin{Bmatrix} t_n \\ t_s \\ t_t \end{Bmatrix} = \begin{bmatrix} K_{\text{nn}} & K_{\text{ns}} & K_{\text{nt}} \\ K_{\text{ns}} & K_{\text{ss}} & K_{\text{st}} \\ K_{\text{nt}} & K_{\text{st}} & K_{\text{tt}} \end{bmatrix} \begin{Bmatrix} \delta_n \\ \delta_s \\ \delta_t \end{Bmatrix} = \mathbf{K}\boldsymbol{\delta}, \tag{21}$$

where $\mathbf{t}$ is the nominal traction vector consisting of three components: normal traction t_n and shear tractions t_s and t_t. Also, $\boldsymbol{\delta}$ and $\mathbf{K}$ are the separation vector and the elastic constitutive matrix, respectively. An uncoupled traction-separation law is employed in this work, in which normal and tangential stiffness components are assumed to be independent terms. This uncoupled behavior implies that a pure normal separation does not cause the development of forces in the shear directions and a shear slip does not create normal cohesive forces. This leads to zero off-diagonal elements of the stiffness matrix and thereby only the diagonal components K_{nn}, K_{ss}, and K_{tt} must be determined. Thus, (21) is reduced to

$$\mathbf{t} = \begin{Bmatrix} t_n \\ t_s \\ t_t \end{Bmatrix} = \begin{Bmatrix} K_{\text{nn}}\delta_n \\ K_{\text{ss}}\delta_s \\ K_{\text{tt}}\delta_t \end{Bmatrix}. \tag{22}$$

Fig. 17 shows the arrangement of wires, together with the conforming mesh used for creating 3D FE models of wire bundles with 7, 12, and 19 wires of type 3 (L = 114 mm). In these meshes, 8-node hexahedral solid elements, 4-node rectangular shell elements, and surface-based cohesive contact are employed to model the wires, tape, and the adhesion along their interfaces, respectively [41]. The reduced integration scheme is used in the solid and shell elements to reduce the computational cost and shear locking effects.

5.2. Explicit dynamic FE analysis

The cantilever bending test of a taped wire bundle can be modeled as a quasi-static phenomenon in a 3D FE simulation. However, the highly nonlinear behavior of the wire bundle, governed by plastic deformation, contact-friction, tape-wire cohesion, and geometrical nonlinearity, could prohibit the convergence of such a simulation using an implicit time integration scheme [26]. This is due to the very small time increment needed to solve the system of equations at each step, which could become smaller than the machine precision and cause convergence difficulties [42]. It has been shown that with special considerations, an explicit dynamic approach can accurately simulate highly nonlinear problems that fail to converge using an implicit scheme [43]. Note that in order to achieve convergence, it is essential to employ an explicit time integration scheme to simulate the mechanical behavior of taped wire bundles subject to bending loads.

By neglecting the effect of viscous damping, the equilibrium equation for solving an explicit dynamic problem can be written as [44,45]

$$\mathbf{M}\ddot{\mathbf{u}} = \mathbf{F}_{\text{ext}} - \mathbf{F}_{\text{int}}, \tag{23}$$

where $\mathbf{M}$ is the mass matrix, $\ddot{\mathbf{u}}$ is the acceleration vector, and $\mathbf{F}_{\text{ext}}$ and $\mathbf{F}_{\text{int}}$ are the external and internal force vectors, respectively. Using the central difference time integration scheme, variations of the velocity vector $\dot{\mathbf{u}}$ can be approximated as [45]

$$\dot{\mathbf{u}}^{t+\frac{\Delta t}{2}} = \dot{\mathbf{u}}^{t-\frac{\Delta t}{2}} + \frac{\left(\Delta t^{t+\Delta t} + \Delta t^{t}\right)}{2}\ddot{\mathbf{u}}^{t}, \tag{24}$$

where t is the current time and Δt is the corresponding time increment. The displacement vector at the end of the time increment is then evaluated as

$$\mathbf{u}^{t+\Delta t} = \dot{\mathbf{u}}^{t} + \Delta t^{t+\Delta t}\left(\ddot{\mathbf{u}}^{t+\frac{\Delta t}{2}}\right). \tag{25}$$

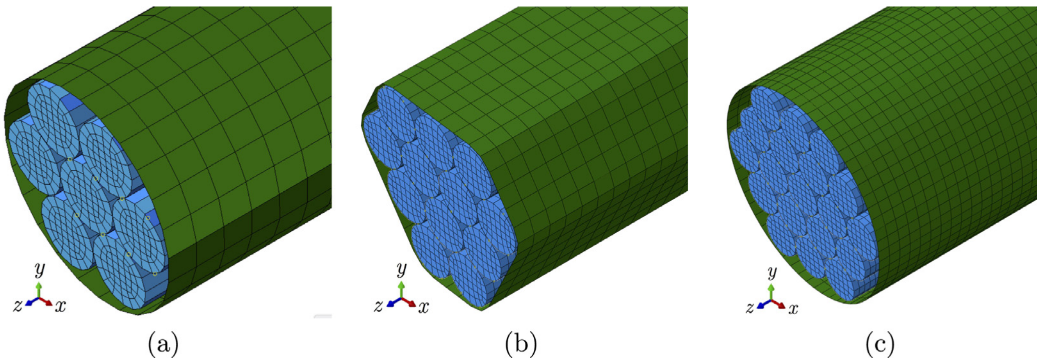

Fig. 17. Internal structure and the FE meshes created for modeling wire bundles composed of (a) 7 wires, (b) 12 wires, and (c) 19 wires of type 3.

Because the central difference method is a conditionally stable algorithm, the maximum time increment is bounded by the stability limit known as the Courant criterion expressed as [45]

$$\Delta t_{\text{stable}} = \frac{2}{\omega_{\max}}, \tag{26}$$

where $\omega_{\max}$ is the highest frequency of the system. Since the exact evaluation of $\omega_{\max}$ is not computationally feasible during an FE simulation, one can approximate the highest frequency of a system by relating that to the size of elements. The stability limit can then be redefined based on the smallest characteristic length of the element increment L_e as

$$\Delta t_{\text{stable}} = \frac{L_e}{C_d}, \tag{27}$$

where C_d is the dilatational wave speed given by

$$C_d = \sqrt{\frac{E}{\rho}}, \tag{28}$$

where ρ is the material density. Note that (27) yields a smaller value for Δt_{stable} than the Courant equation given in (26).

One of the main challenges in simulating highly nonlinear mechanical behaviors using an explicit approach is to achieve a sufficiently large Δt_{stable}, which according to (27) and (29) has a direct relationship with $\sqrt{\rho}$. One approach commonly used for increasing Δt_{stable} in such problems is to artificially increase the density using a mass scaling factor f_m as

$$\rho' = f_m \rho. \tag{29}$$

Note that the body forces associated with the weights of wires are not affected by this mass scaling. While introducing f_m increases Δt_{stable} and thereby reduces the computational cost, it also has the side effect of magnifying the mass matrix **M**, which in turn leads to an increase in the inertial forces in the system. In other words, using an excessively large f_m for simulating a quasi-static problem results in unfeasibly high dynamic effects that severely undermines the accuracy. Thus, to determine an appropriate value for f_m that provides an acceptable balance between the computational cost and accuracy, one must monitor the ratio of the kinetic to internal energies throughout the simulation. A mass scaling factor can be incorporated in the simulation only if this ratio is sufficiently small (in this work, less than 5%).

Another challenge toward the high-fidelity FE simulation of the mechanical behavior of taped wire bundles using bilinear (8-node hexahedral) elements is the so-called hourglass effect [46]. While using a reduced integration scheme in such elements can reduce the computational time and avoid shear-locking [47], it also gives rise to non-physical, zero energy modes (hourglass modes), which deteriorate the accuracy by disturbing the actual response of the system. This effect can be characterized by monitoring the artificial strain ene.g. [41], which, similar to the kinetic energy, must be considerably smaller than the internal energy to yield an acceptable accuracy. If a high hourglass effect is detected, the finite element mesh must be refined more to reduce this effect. In the FE simulations presented next, several numerical tests are performed and both the kinetic and artificial strain energies are monitored to identify appropriate value of the mass scaling factor and the mesh size for each simulation. It must be noted that due to the large number of degrees of freedom and highly nonlinear nature of the problem, all high-fidelity simulations presented next are conducted on a massively parallel computing platform.

5.3. Calibration of high-fidelity FE models

While the effective elastoplastic properties of electrical wires and tape are evaluated based on experimental data, performing tests to quantify the adhesion stiffness K_{cc} between the tape and wires, as well as the friction coefficient μ between the wires, would be a challenging task. Instead, these parameters can be evaluated by calibrating the high-fidelity FE simulation of the cantilever bending test of a taped wire bundle with the corresponding experimental data. Details regarding the implementation of cohesive interaction and proper selection of corresponding stiffness values are provided in several references including [41,48]. Here, the normal $K_{nn} = K_{cc}$, shear K_{ss}, and tangential K_{tt} cohesive stiffness values are related to one another as $K_{ss} = K_{tt} = \frac{1}{3} K_{cc}$.

After a comprehensive numerical study, a time period of $t = 1$ s and a mass scaling factor of $f_m = 25$ were selected to ensure that dynamic effects are negligible in the explicit dynamic simulations. To better understand the effect of the mass scaling factor on the computational efficiency, note that the stable time increment needed to simulate the deformation response of the 7-wire bundle shown in Fig. 17a with $f_m = 1$ is $\Delta t_{\text{stable}} = 6.887 \times 10^{-8}$ s. Using a small mass scaling factor of $f_m = 25$, the stable time increment can be increased to $\Delta t_{\text{stable}} = 3.443 \times 10^{-7}$ s. This decreases the computing time from 627 min to 181 min (approximately 71% reduction) when the simulation is performed on 180 Intel Xeon X5650 CPUs (Westmere-EP, 6 cores, 2.67 GHz).

As the first step of the calibration, a parametric study was conducted to determine the appropriate values of K_{cc} and μ by comparing the simulations with the average of experimentally measured force-deflection responses of the taped wire bundle samples composed of 7 wires. The results of this study are summarized in Fig. 18, showing that the simulation results are not highly sensitive to the value of μ. Also, except for $K_{cc} = 30$ N/mm^3, no meaningful variation can be observed in the simulated force-deflection curves for different cohesive stiffness values. In other words, if K_{cc} is selected sufficiently large to hold the wires together during the simulation (as observed in the experiments), its value has no considerable impact on the simulation results. This parametric study shows that $\mu = 0.4$ and $K_{cc} = 30$ N/mm^3 can be selected as best estimates for these parameters.

To ensure that the values calibrated for μ and K_{cc} based on the experimental data associated with the 7-wire bundle are suitable, these values are utilized to simulate the cantilever bending of wire bundles composed of 12 and 19 wires. A comparison between the simulated and experimentally measured force-deflection responses is presented in

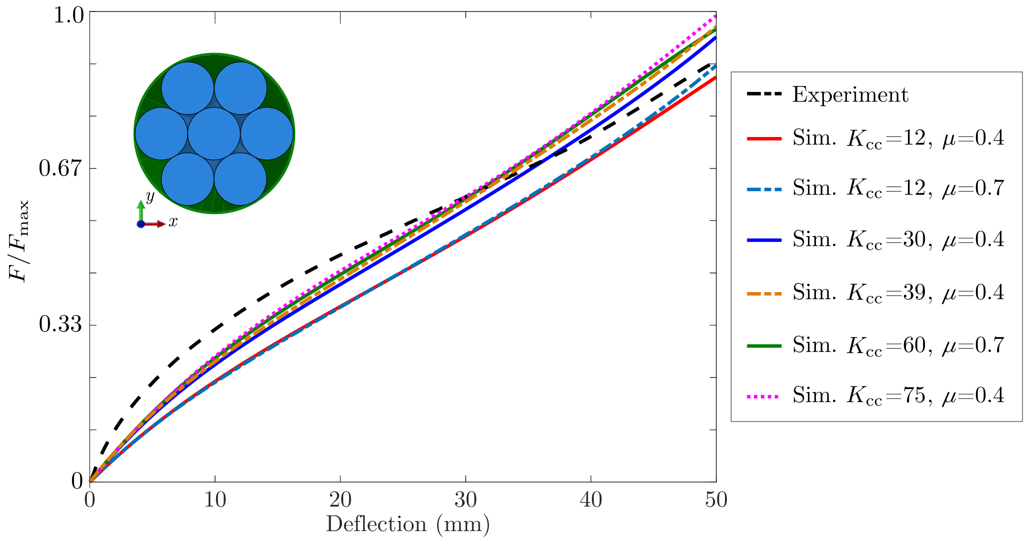

Fig. 18. Calibration of the friction coefficient μ between the wires and the cohesive contact stiffness K_{cc} (N/mm^3) used for modeling the adhesion between the tape and wires in a 7-wire bundle.

Fig. 19. This figure shows a good match between both curves up to a deflection of $\delta = 35$ mm, after which the FE results deviate from the experimental curves. The initial mismatch between the simulation and test results at small deflections is particularly due to the simplified constitutive model selected for single composite wires. A comprehensive study was carried out to re-calibrate μ and K_{cc}, which showed that the values obtained based on the experimental data for the 7-wire bundle ($\mu = 0.4$ and $K_{cc} = 30$ N/mm^3) would indeed be the best estimates for these parameters. Even introducing damage (debonding) along the wire-tape interfaces in the FE models did not have desired impacts on the deformation responses of the wire bundles.

Further analysis of the behavior of the taped wire bundles during the cantilever bending tests revealed that the discrepancy between experimental and simulation results at large deflection could be due to the slip-friction between wires. Thus, a dynamic friction model was adopted to simulate the relative sliding of wires by reducing the friction coefficient at higher deflections. A new calibration study was then conducted on bundles of 12 and 19 wires, which indicated that $\mu_s = 0.4$ (same value obtained based on 7-wire bundle test results), $\mu_k = 0.1$, and $d_c = 2$ in (20) are appropriate values for these parameters. The force-deflection curves obtained from the new FE analyses relying on this dynamic friction model are also illustrated in Fig. 19, which shows a better correlation with experimental data. Note that, as shown in this figure, introducing the dynamic friction to the FE models also yields a better match between the experimental and simulated force-deflection responses of the 7-wire bundle. The error curves between average experimental and 3D simulation results presented in Fig. 19 are illustrated in Fig. 20, together with corresponding *RMS* values, which are varying between 2.45×10^{-2} and 6.53×10^{-2}.

Fig. 21 illustrates the FE simulation of the deformed shape of the wire bundle with 12 wires of type 3. Note that despite using a mass scaling factor and selective reduced integration in this explicit dynamic simulation, no mesh distortion or oscillation is observed in this figure, which indicates the soundness of the results. Fig. 22 further verifies this observation by showing the small ratio of the artificial strain and kinetic energies compared to the internal energy in the FE analyses of all three wire bundles, indicating that hourglass and dynamic effects are negligible. Thus, this figure reassures that using $f_m = 25$ with the reduced integration scheme in the high-fidelity models can properly replicate the quasi-static deformation response of wire bundles during cantilever bending tests.

5.4. Validation of high-fidelity FE models

In order to validate the high-fidelity FE model of wire bundles calibrated with experimental data corresponding to bundles of 7, 12, and 19 wires, this model was implemented to simulate the deformation responses of the wire bundles shown in Fig. 23. The first bundle is composed of 27 wires of type 3 with a hexagonal cross-section, while the 19-wire bundle is composed of 10 wires of type 3 and 9 wires of type 2. Fig. 23 also shows portions of the meshes used for creating the FE model of each taped wire bundle, which have similar features to the meshes used in Section 5.3 for the calibration study. The simulated deformed shapes of these wire harnesses during the cantilever bending are depicted in Fig. 24, showing no distortion in the mesh. The kinetic and artificial strain energies associated with these simulations were verified to be negligible compared to the internal energy of the system throughout the simulation. As illustrated in Fig. 24, using a dynamic friction model to simulate the wires interaction allows some of them to slide out of the bundle, which is similar to the behavior observed in the cantilever bending tests.

Fig. 25 provides a comparison between the experimental and simulated force-deflection responses of the taped wire bundles depicted in Fig. 23. This figure illustrates the results for both the static and dynamic models for friction between wires, reassuring that the latter can more accurately simulate the physical behavior of the bundle. Despite the uncertainty associated with the presence of residual stresses in the individual wires, as well as the variability in the construction of taped wire bundles, the simulated force-deflection response of the mixed 19-wire bundle shown in Fig. 25a shows a good match with the experimental results over a wide range of deformation.

For the results of the 27-wire bundle depicted in Fig. 25b, a softening behavior is observed in the experimental curves after a deflection of $\delta = 30$ mm. The effects of different FE model variations were studied, including allowing debonding along tape-wire interfaces and modifying the dynamic friction model to allow sliding between wires with no friction at higher deformations. While the difference between the numerical and experimental results decreased slightly, none of these changes produced the experimental softening behavior shown in Fig. 25b. Further analysis of the experimental tests showed that the softening characteristic of the 27-wire bundle, which is not observed in the tests conducted on other wire bundles, is due to the slippage between wires and the tape. After this slippage, the load applied by the aramid strain is only sustained by the tape. This phenomenon undermines the integrity of the

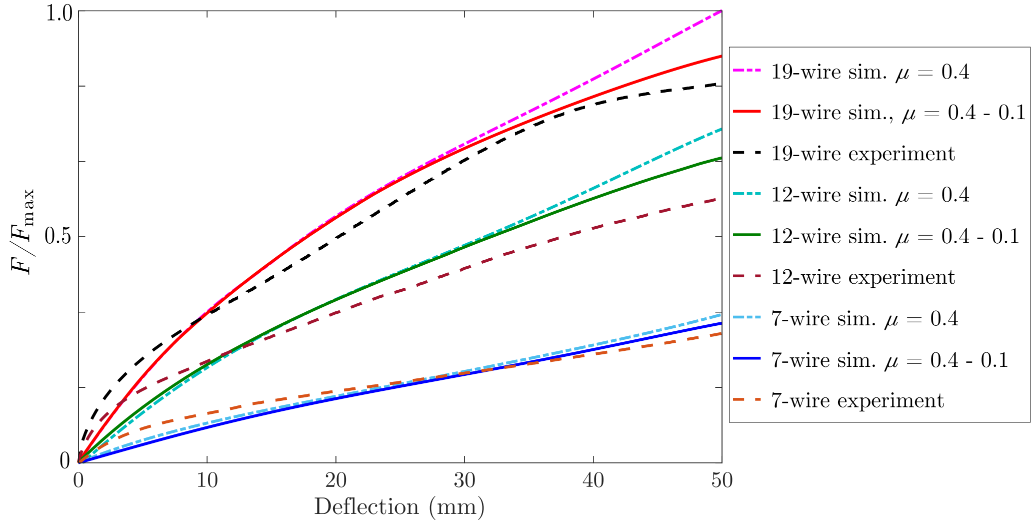

Fig. 19. Force-deflection responses of cantilevered taped wire bundles made of type 3 wires, where 3D FE simulations with a constant friction coefficient of $\mu = 0.4$ and dynamic friction coefficients ranging from μ_s=0.4 to μ_f=0.1 between the wires are compared with the corresponding average experimental results.

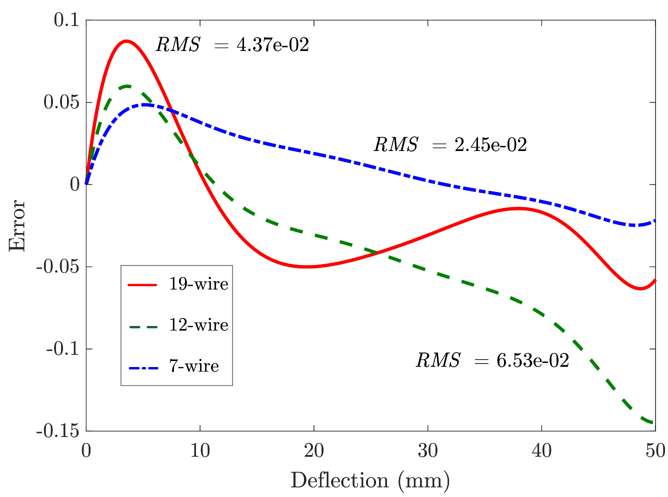

Fig. 20. Error curves between the average experimental and 3D FE simulated force-deflection responses shown in Fig. 19 for the taped wire bundles made of type 3 wires. *RMS* values of the error are also reported for each curve.

structure, which leads to a softening behavior due to localized plastic deformations that cannot be captured by the FE model. Nevertheless, given the presence of other sources of uncertainty including residual stresses, Fig. 25b shows an acceptable match between the experimental and simulated force-deflection responses of the 27-wire bundle for deflections lower than $\delta = 30$ mm.

5.5. Effective properties for 1D FE models

As noted previously, the high-fidelity FE model of taped wire bundles can serve as a surrogate for physical testing to obtain the data needed to characterize their effective elastoplastic properties. The effective diameter of a circular 1D beam representing a taped wire bundle is the outer diameter of the cylinder circumscribing the taped wire bundle. The density of this homogenized model is evaluated using the rule of mixtures as

$$(\rho A)_{\text{eff}} = (\rho A)_{\text{wires}} + (\rho A)_{\text{tape}}. \tag{30}$$

Table 4 gives the effective diameters and effective densities of the taped wire bundles.

Using the force-deflection responses obtained from the 3D simulations of the cantilever bending, we reutilized the optimization-based algorithm described in Section 4.1 to evaluate the homogenized properties of the wire bundles, which are summarized in Table 5. Using the rule of mixtures, an average effective Poisson's ratio of $\nu_{\text{eff}} = 0.3$ is evaluated for all reduced-order models of taped wire bundles. Fig. 26 illustrates a comparison between the simulated force-deflection curves using the high-fidelity 3D model and reduced-order 1D FE models relying on these effective elastoplastic properties. While the computational cost associ-

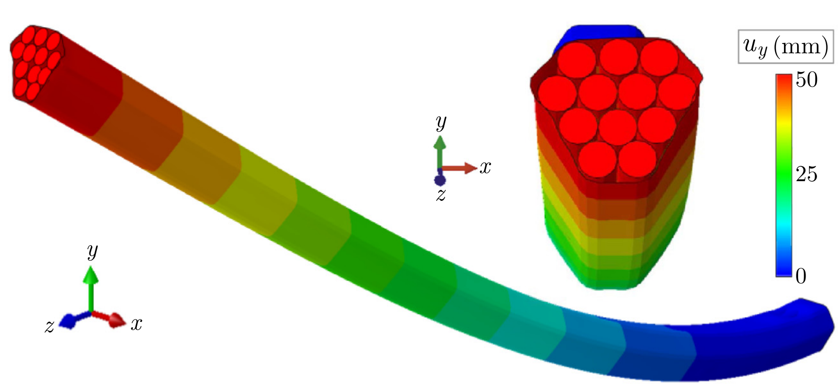

Fig. 21. 3D FE simulation of the deformed shape of the 12-wire bundle of type 3.

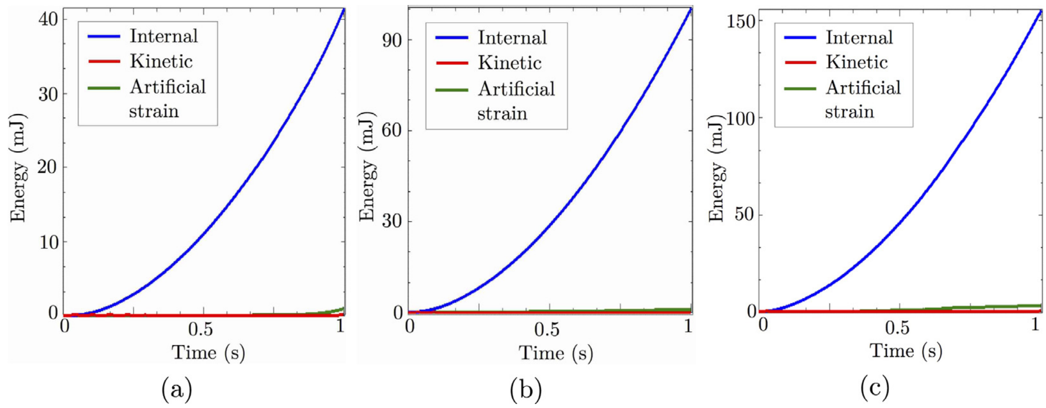

Fig. 22. Variations of the internal, artificial strain, and kinetic energies versus time during the explicit dynamic FE simulation of the deformation response of cantilevered taped wire bundles composed of (a) 7 wires, (b) 12 wires, and (c) 19 wires of type 3.

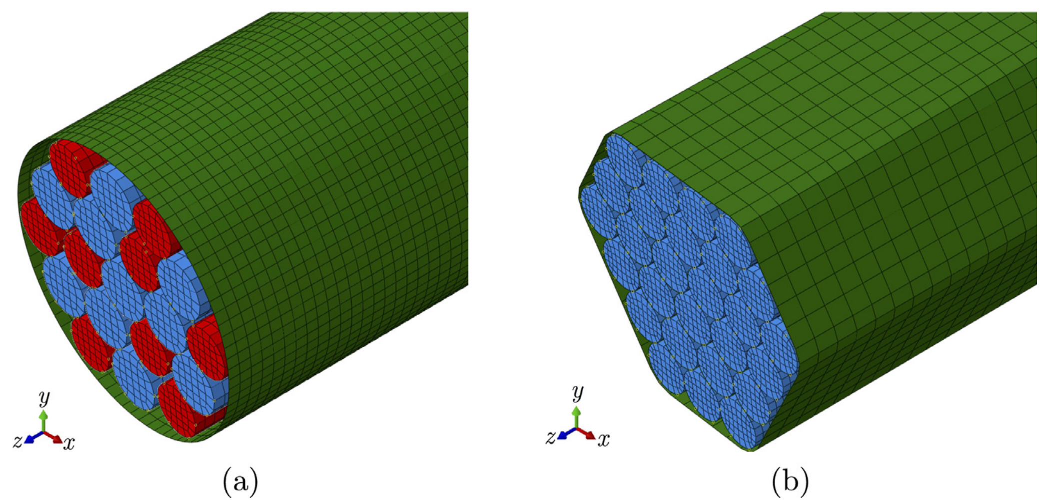

Fig. 23. Internal structure and the FE meshes created for modeling wire harnesses composed of (a) 19 mixed wires of types 2 and 3 and (b) 27 wires of type 3.

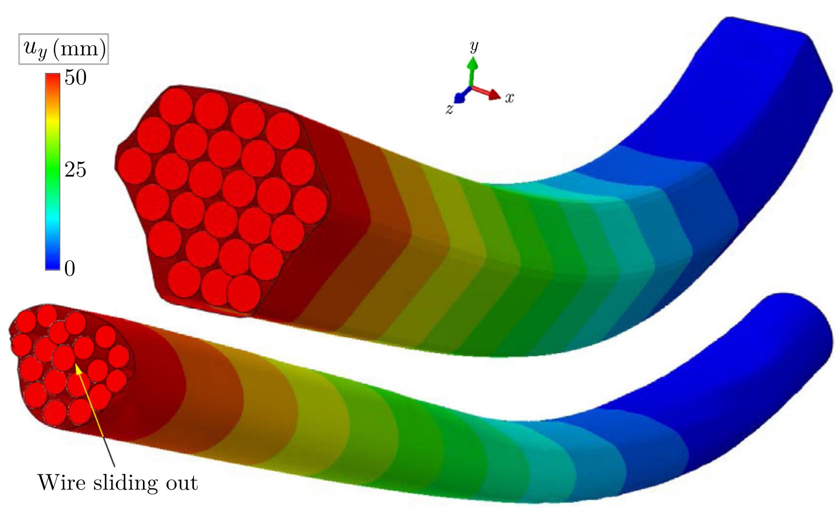

Fig. 24. 3D FE simulations of the deformation responses of taped wire bundles composed of 27 wires of type 3 (top) and 19 mixed wires of types 2 and 3 (bottom).

ated with these 1D simulations is less than 0.5% of that corresponding to high-fidelity simulations, as shown in this figure, both models yield nearly identical results. Thus, provided that plasticity is taken into account and the effective material properties are calibrated properly, a 1D FE model can reliably predict the deformation response of taped wire bundles subject to bending loads.

6. Conclusion

A synergistic computational-experimental approach was presented to characterize the mechanical behavior of electrical wires and taped wire bundles in bending. Numerical and experimental studies showed that, although not taken into account in most digital manufacturing soft-

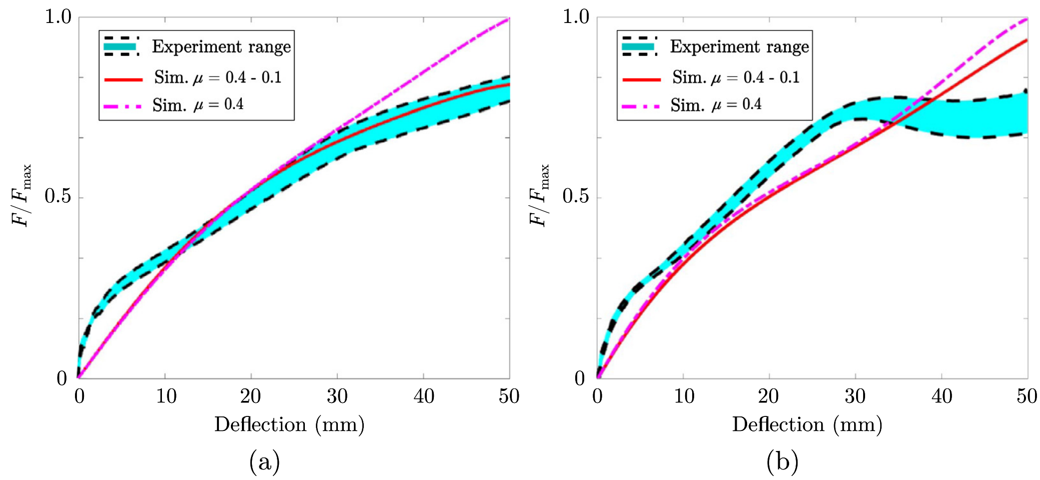

Fig. 25. Comparison between experimental and 3D FE simulated force-deflection responses of cantilevered taped wire bundles composed of (a) 19 wires of types 2 and 3; (b) 27 wires of type 3. The experimental ranges are based on the results from three samples.

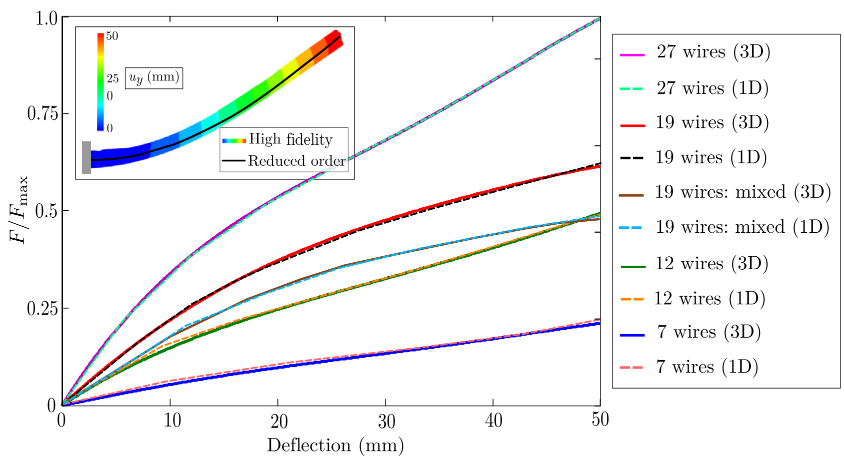

Fig. 26. Comparison between the force-deflection response of the cantilevered taped wire bundles predicted using the 3D and 1D FE models. The inset of the figure compares the resulting simulated bent shapes of the 19-wire bundle of type 3.

Table 4
Effective diameters (d_o) and densities (ρ) of the reduced order models of taped wire bundles.

Wire bundle	d_o (mm)	ρ (g/cm^3)
7 wires (type 3)	4.6	3.43
12 wires (type 3)	5.8	3.65
19 wires (type 3)	7.4	3.50
19 wires (types 2 & 3)	7.4	3.00
27 wires (type 3)	9.2	3.20

Table 5
Effective elastoplastic properties of the taped wire bundles calibrated with the high-fidelity 3D FE results using the optimization-based algorithm.

Wire bundle	E (MPa)	σ_Y (MPa)	K (MPa)	n
7 wires (type 3)	1,114	2.70	544.9	0.92
12 wires (type 3)	1,022	3.12	75.1	0.50
19 wires (type 3)	616	2.40	15.0	0.32
19 wires (types 2 & 3)	442	1.72	7.8	0.26
27 wires (type 3)	449	2.17	41.6	0.65

ware packages, plasticity has a significant impact on the deformed shape of wires subjected to bending loads. Also, the internal structures of wires and residual stresses could have a notable impact on the their mechanical behavior of wires in bending. A customized cantilever bending test was developed to characterize the deformed shapes and force-deflection responses of single wires and taped wire bundles. The experimental data was then used with an optimization-based algorithm to evaluate the corresponding effective elastoplastic properties. A high-fidelity 3D FE model was also introduced for simulating the mechanical behavior of taped wire bundles, which can serve as a surrogate for experimental testing. In addition to the effective elastoplastic properties of wires and tapes, the dynamic friction coefficients between wires and the cohesive bonding stiffness along tape-wire interfaces were calibrated with experimental data. This study showed that 1D FE models relying on homogenized elastoplastic properties can accurately simulate the deformation responses of electrical wires and taped wire bundles subject to bending loads.

Acknowledgment

This work was funded by Honda R&D Americas, Inc. and also in part by an allocation of computing time from the Ohio Supercomputer Center (OSC) and the Ohio State University Simulation Innovation and Modeling Center (SIMCenter).

References

[1] Antman SS. Problems in nonlinear elasticity. Nonlinear Probl Elast 2005:513–84.
[2] Grégoire M, Schömer E. Interactive simulation of one-dimensional flexible parts. Comput-Aided Des 2007;39(8):694–707.
[3] Brand M, Rubin MB. A constrained theory of a cosserat point for the numerical solution of dynamic problems of non-linear elastic rods with rigid cross-sections. Int J Non Linear Mech 2007;42(2):216–32.
[4] Jeong IK, Lee I. An oriented particle and generalized spring model for fast prototyping deformable objects. In: Alexa M, Galin E, editors. In: Eurographics 2004 - Short Presentations. Eurographics Association; 2004. doi:10.2312/egs.20041014.
[5] Ghoreishi SR, Cartraud P, Davies P, Messager T. Analytical modeling of synthetic fiber ropes subjected to axial loads. part i: a new continuum model for multilayered fibrous structures. Int J Solids Struct 2007;44(9):2924–42.
[6] Y Yu Y, Wang X, Chen Zh. A simplified finite element model for structural cable bending mechanism. Int J Mech Sci 2016;113:196–210.
[7] Wu W, Cao X. Mechanics model and its equation of wire rope based on elastic thin rod theory. Int J Solids Struct 2016;102:21–9.
[8] Zhu ZH, Meguid SA. Nonlinear fe-based investigation of flexural damping of slacking wire cables. Int J Solids Struct 2007;44(16):5122–32.
[9] Argatov I. Response of a wire rope strand to axial and torsional loads: asymptotic modeling of the effect of interwire contact deformations. Int J Solids Struct 2011;48(10):1413–23.
[10] Spak K, Agnes G, Inman D. Cable modeling and internal damping developments. Appl Mech Rev 2013;65(1):010801.
[11] Howell LL. Compliant mechanisms. John Wiley & Sons; 2001.
[12] Wakamatsu H, Hirai Sh. Static modeling of linear object deformation based on differential geometry. Int J Rob Res 2004;23(3):293–311.
[13] Theetten A, Grisoni L, Andriot C, Barsky B. Geometrically exact dynamic splines. Comput-Aided Des 2008;40(1):35–48.
[14] Gautam M, Katnam KB, Potluri P, Jha V, Latto J, Dodds N. Hybrid composite tensile armour wires in flexible risers: a multi-scale model. Compos Struct 2017;162:13–27.
[15] Nemov AS, Boso DP, Voynov IB, Borovkov AI, Schrefler BA. Generalized stiffness coefficients for iter superconducting cables, direct fe modeling and initial configuration. Cryogenics 2010;50(5):304–13.
[16] Nikitin I, Nikitina L, Frolov P, Goebbels G, Göbel M, Klimenko S, et al. Real-time simulation of elastic objects in virtual environments using finite element method and precomputed greens functions. In: Eighth eurographics workshop on virtual environments; 2002. p. 47–52.
[17] Stanova E, Fedorko G, Fabian M, Kmet S. Computer modelling of wire strands and ropes part ii: finite element-based applications. Adv Eng Software 2011;42(6):322–31.
[18] Griffith JH, Bragg JG. Strength and other properties of wire rope, 121. US Govt. Print. Off.; 1919.
[19] Elata D, Eshkenazy R, Weiss MP. The mechanical behavior of a wire rope with an independent wire rope core. Int J Solids Struct 2004;41(5):1157–72.
[20] Papailiou KO. On the bending stiffness of transmission line conductors. IEEE Trans Power Delivery 1997;12(4):1576–88.
[21] Filiatrault A, Stearns C. Flexural properties of flexible conductors interconnecting electrical substation equipment. J Struct Eng 2005;131(1):151–9.
[22] Van der Heijden GHM, Neukirch S, Goss VGA, Thompson JMT. Instability and self-contact phenomena in the writhing of clamped rods. Int J Mech Sci 2003;45(1):161–96.
[23] Goss VGA, Van der Heijden GHM, Thompson JMT, Neukirch S. Experiments on snap buckling, hysteresis and loop formation in twisted rods. Exp Mech 2005;45(2):101–11.
[24] Dörlich V, Linn J, Scheffer T, Diebels S. Towards viscoplastic constitutive models for cosserat rods. Arch Mech Eng 2016;63(2):215–30.
[25] Wright RN. Wire technology: process engineering and metallurgy. Butterworth-Heinemann; 2016.
[26] Bathe KJ. Finite element procedures. Klaus-Jurgen Bathe; 2006.
[27] Groover MP. Automation, production systems, and computer-integrated manufacturing. Prentice Hall Press; 2007.
[28] Simo JC, Hughes TJR. Computational inelasticity, volume 7 of interdisciplinary applied mathematics; 1998.
[29] Khan AS, Huang S. Continuum theory of plasticity. John Wiley & Sons; 1995.
[30] Jirásek M, Bazant ZP. Inelastic analysis of structures. John Wiley & Sons; 2002.
[31] Zienkiewicz OC, Taylor RL, Zhu JZ. The finite element method: its basis and fundamentals. Elsevier; 2005.
[32] Jones RM. Mechanics of composite materials. CRC press; 1998.
[33] Schajer GS. Measurement of non-uniform residual stresses using the hole–drilling method. Part i stress calculation procedures. J Eng Mater Technol 1988;110(4):338–43.
[34] Amouzegar H, Schafer BW, Tootkaboni M. An incremental numerical method for calculation of residual stresses and strains in cold-formed steel members. Thin-Walled Struct 2016;106:61–74.
[35] Sadd MH. Elasticity: theory, applications, and numerics. Academic Press; 2009.
[36] Hosford WF, Caddell RM. Metal forming: mechanics and metallurgy. Cambridge University Press; 2011.
[37] Chakrabarty JA. Applied plasticity, Vol. 88. Springer; 2000.
[38] Nelder JA, Mead R. A simplex method for function minimization. Comput J 1965;7(4):308–13.
[39] Lagarias JC, Reeds JA, Wright MH, Wright PE. Convergence properties of the nelder–mead simplex method in low dimensions. SIAM J Optim 1998;9(1):112–47.
[40] Oden JT, Martins JAC. Models and computational methods for dynamic friction phenomena. Comput Methods Appl Mech Eng 1985;52(1–3):527–634.
[41] Systemès D. Abaqus version 6.14, user documentation. Dassault Systemes, Providence, RI; 2014.
[42] Bathe KJ, Cimento AP. Some practical procedures for the solution of nonlinear finite element equations. Comput Methods Appl Mech Eng 1980;22(1):59–85.
[43] Chung WJ, Cho JW, Belytschko T. On the dynamic effects of explicit fem in sheet metal forming analysis. Eng Comput 1998;15(6):750–76.
[44] Hughes TJR. The finite element method: linear static and dynamic finite element analysis. Courier Corporation; 2012.
[45] De Borst R, Crisfield MA, Remmers JJC, Verhoosel CV. Nonlinear finite element analysis of solids and structures. John Wiley & Sons; 2012.
[46] Belytschko T, Ong JSJ, Liu WK, Kennedy JM. Hourglass control in linear and nonlinear problems. Comput Methods Appl Mech Eng 1984;43(3):251–76.
[47] Zienkiewicz OC, Taylor RL. The finite element method for solid and structural mechanics. Butterworth-Heinemann; 2005.
[48] Turon A, Davila CG, Camanho PP, Costa J. An engineering solution for mesh size effects in the simulation of delamination using cohesive zone models. Eng Fract Mech 2007;74(10):1665–82.